Urban Water Journal, 2015
Vol. 12, No. 6, 502–518, http://dx.doi.org/10.1080/1573062X.2013.847464

Taylor & Francis
Taylor & Francis Group

RESEARCH ARTICLE

Air entrainment and turbulent fluctuations in hydraulic jumps

H. Wang and H. Chanson*

School of Civil Engineering, The University of Queensland, Brisbane QLD 4072, Australia

(*Received 5 February 2013; accepted 12 September 2013*)

A hydraulic jump is the sudden transition from a high-velocity impinging flow into a turbulent roller in an open channel. Substantial amounts of air are entrapped at the impingement point, and significant free-surface fluctuations take place above the roller. In the present study, some physical modelling was conducted in a relatively large sized facility. The flow conditions included a wide ranges of inflow Froude numbers and Reynolds numbers ($3.8 < Fr_1 < 10.0$, $2.1 \times 10^4 < Re < 1.6 \times 10^5$). The fluctuating features of free-surface and roller position were investigated non-intrusively with a series of acoustic displacement meters. The characteristic frequencies of the fluctuating motions were documented, and some major roller surface deformation patterns were revealed. The air-water flow properties were investigated with an intrusive phase-detection probe. The void fraction and bubble count rate data were documented in the jump roller, together with the interfacial velocity distributions. The rate of air entrainment was estimated based upon the void fraction and interfacial velocity distribution data. Some simultaneous measurements of instantaneous void fraction and free-surface fluctuations as well as longitudinal jump front oscillations were conducted. The relationship between the rate of air entrainment and turbulent fluctuations is discussed. Both the turbulent fluctuation and aeration properties are basic design parameters in urban water systems in which a hydraulic jump may take place. The present work provides relevant information for water systems including covered channels and partially-filled pipes.

Keywords: hydraulic jumps; turbulent fluctuations; air entrainment; free-surface fluctuations; physical modelling

1. Introduction

A hydraulic jump is an abrupt transition from a supercritical to subcritical free-surface flow, associated with a turbulent roller (Henderson 1966, Liggett 1994). The jump roller is characterised by spray and splashing with a highly fluctuating free-surface, together with highly-aerated turbulent flow structures within. Besides in rivers and streams, a hydraulic jump is also commonly experienced in open hydraulic structures, urban sewage systems and water treatment plants as an energy dissipator, flow aerator and mixer (Figure 1). Figure 1 shows a hydraulic jump in an irrigation channel. The flow regime is complex considering the turbulent, two-phase flow features which are not fully understood to date (Rajaratnam 1967, Chanson 2009).

The application of momentum principle to a hydraulic jump in a horizontal, rectangular channel yields the ratio of conjugate depths (Bélanger 1841):

$$\frac{d_2}{d_1} = \frac{1}{2} \times \left(\sqrt{1 + 8 \times Fr_1} - 1 \right) \quad (1)$$

where d is water depth and the subscripts 1 and 2 refer to the upstream and downstream flow conditions respectively and Fr_1 is the inflow Froude number defined as $Fr_1 = V_1/(g \times d_1)^{1/2}$, with V_1 the average inflow velocity and g the gravity acceleration (Figure 2). For the physical modelling of a hydraulic jump, a large number of parameters are relevant to the study of hydraulic jumps (Liggett 994). The Froude similarity is implied by the momentum considerations (Lighthill 1978, Liggett 1994, Chanson 2012). Dimensional considerations suggest that the Reynolds number $\mathrm{Re} = \rho \times V_1 \times d_1/\mu$, is another relevant dimensionless number, where ρ and μ are the density and dynamic viscosity of water (Chanson 2007b, Chanson and Gualtieri 2008). However, a dynamic similitude with identical Froude and Reynolds numbers cannot be fulfilled if the same fluids are used in model and prototype. Drastic scale effects were shown in terms of air entrainment and turbulent dissipation in hydraulic jumps with Froude similitude but different Reynolds numbers (Chanson and Gualtieri 2008, Chanson and Chachereau 2013).

Experimental studies of hydraulic jumps focusing on detailed two-phase flow measurements dated back to Rajaratnam (1962). The influence of inflow conditions on bubble entrainment process was highlighted by Resch and Leutheusser (1972). With partially-developed inflow conditions, Chanson (1995) developed an analogy between the air entrainment process in hydraulic jumps and that in plunging jets. Systematic investigations using intrusive phase-detection probes were conducted by

*Corresponding author. Email: h.chanson@uq.edu.au

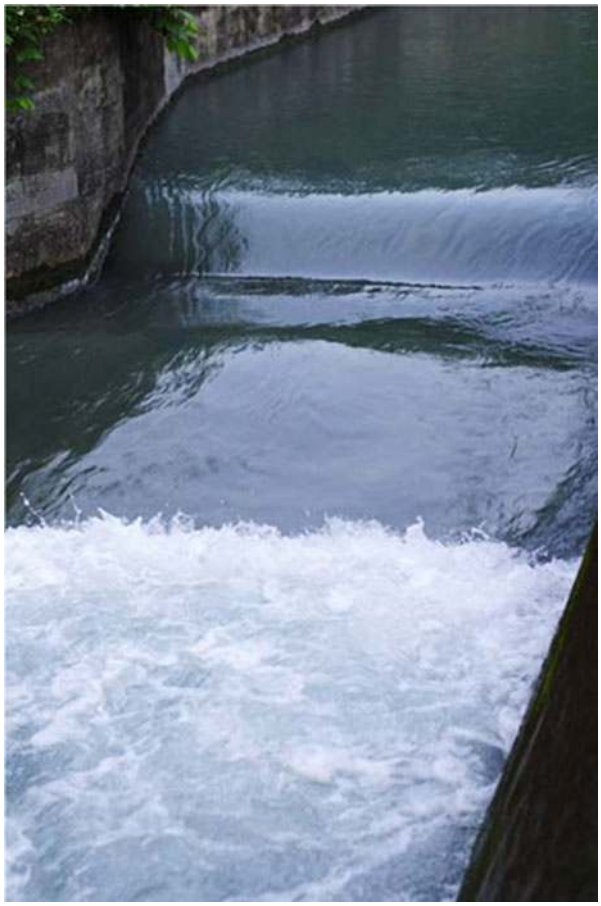

Figure 1. Hydraulic jump in a man-made water supply channel in November 2010.

Chanson and Brattberg (2000), Murzyn *et al.*, (2005) and Chanson (2007a, 2010). Air-water flow properties including void fraction, bubble count rate and interfacial velocity were presented. New insights into turbulent level and coherent time/length scales were provided by Chanson and Carosi (2007) and Zhang *et al.* (2013). The free-surface profile and fluctuations were recently treated using intrusive wire gauges (Mouaze *et al.* 2005, Murzyn *et al.* 2007) and non-intrusive acoustic displacement meters (Murzyn and Chanson 2009, Chachereau and Chanson 2011).

The purpose of this paper is to broaden the knowledge of fluctuating roller free-surface and two-phase flow properties in hydraulic jumps. New experiments were conducted with a wide range of Froude numbers ($3.8 < Fr_1 < 10.0$) and Reynolds numbers ($2.1 \times 10^4 < Re < 1.6 \times 10^5$). The instantaneous free-surface motions were measured non-intrusively in both vertical and horizontal directions, and some surface deformation patterns were defined. The two-phase flow measurement results were presented, some data being collected simultaneously with the free-surface fluctuations. It is the aim of present work to gain better understanding of the interaction between the air entrainment and turbulent fluctuations.

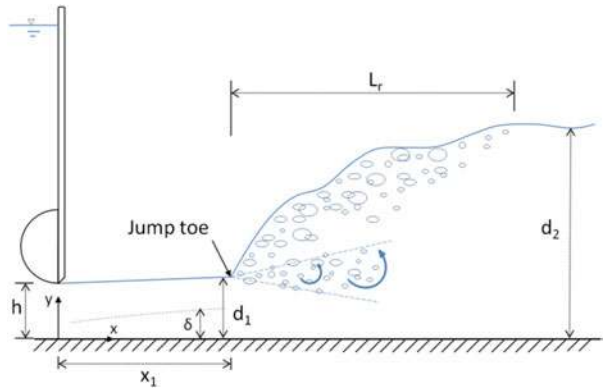

Figure 2. Sketch of the experimental hydraulic jump.

2. Experimental setup and data processing

2.1 Experimental facilities and instrumentation

The experiments were performed in a 3.2 m long horizontal channel with a rectangular cross-section of 0.5 m width. The flow rate was measured with Venturi meters mounted in supply lines and calibrated on site beforehand. The inflow conditions were controlled by a vertical undershoot sluice mounted in a head tank upstream of the channel. A horizontal inflow was generated by a semi-circular ($Ø = 0.3$ m) undershoot gate at the upstream end (Figure 2). The downstream flow conditions were controlled by an overshoot sluice located at the end of channel. A sketch of an experimental hydraulic jump is shown in Figure 2. Some relevant parameters are denoted, including the sluice gate opening h, the inflow water depth d_1 and downstream depth d_2, the longitudinal jump toe position x_1 and the length of jump roller L_r.

The clear-water flow depths were measured with a point gauge. The instantaneous free-surface elevations above the hydraulic jump were recorded using acoustic displacement meters (Microsonic™ Mic + 25/IU/TC and Mic + 35/IU/TC). The displacement meters enabled a non-intrusive measurement of instantaneous water levels by emitting an acoustic beam and receiving the reflected one. The distance between the sensor and detected water surface was derived from the travel time of the beam. The measurement range of Mic + 25/IU/TC sensors was 30 to 250 mm, with an accuracy of 0.18 mm and response time less than 50 ms.

A double-tip phase-detection conductivity probe was used to measure the air-water flow properties. The conductivity probe was an intrusive needle probe discriminating between air and water phases based upon their different electrical conductivities. The double-tip

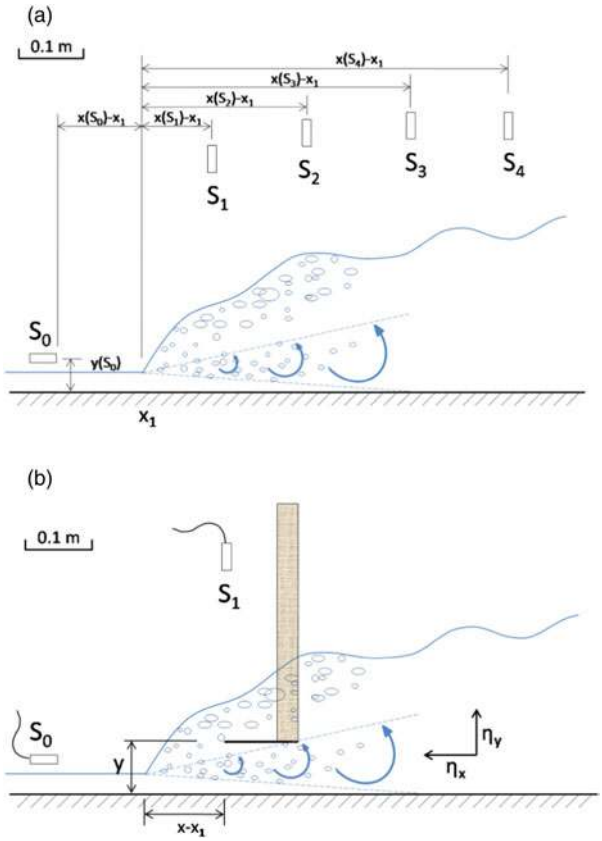

Figure 3. Experimental setups – (a) free-surface measurements; (b) simultaneous free-surface and air-water flow measurements.

probe was equipped with two identical needle sensors with inner diameters $\emptyset = 0.25$ mm. The sensors were mounted parallel with a longitudinal separation distance between the sensor tips $\Delta x_{tip} = 7.46$ mm. The leading and trailing tips were excited simultaneously by an electronic system (model Ref. UQ82.518). The elevation of the probe was supervised by a Mitutoyo^{TM} digimatic scale unit with an accuracy of 0.1 mm.

2.2 Signal processing

The acoustic displacement meters were sampled at 50 Hz for at least 540 s when the free-surface fluctuations were measured alone and at 5 kHz for 180 s when they were used together with the phase-detection probe. The raw output was voltage signals containing some erroneous data mainly caused by (a) the acoustic beam failed to be captured by the sensor because of some angle of the water surface, (b) the acoustic beam reflected by a splashing droplet or a water drop stuck at the sensor head, and (c) some interference by adjacent sensors. The erroneous data resulted in some meaningless spikes in the signal, which were removed using some simple threshold techniques. A sensitivity analysis showed that the standard deviation of post-processed signal was somehow dependent upon the threshold levels. The despiked signals were converted into water depth data based upon to the calibration relationships obtained on-site.

The phase-detection probe was sampled at 20 kHz for 45 s for the air-water flow measurements and at 5 kHz for 180 s for the simultaneous measurements with the acoustic displacement meters. Voltage signals between -1 and 4.5 V were recorded and processed using a single-threshold technique, the threshold being set at 50% of the air-water range. The signal processing followed closely the method of Chanson and Carosi (2007).

The simultaneous sampling of the free-surface elevation and instantaneous void fraction data required further processing, detailed in Section 5.

2.3 Experimental setups and flow conditions

Up to 15 acoustic displacement meters were used simultaneously for the free-surface measurements at various locations, but only the data obtained on the channel centreline are presented in this paper. Figure 3 shows the experimental setups on the channel centreline. In Figure 3a, several displacement meters were mounted above the jump, measuring the free-surface profile and fluctuations. Another sensor was placed horizontally close to the supercritical inflow surface, with the sensor head facing the jump front from upstream. The horizontal jump front motions were measured simultaneously with the free-surface fluctuations. Figure 3b illustrates the simultaneous measurements of free-surface motions and instantaneous void fraction. One vertical and one horizontal displacement meters were used together with the phase-detection probe. The phase-detection probe sensor was operated in various elevations y, and the vertical displacement meter was aligned over the probe leading tip.

Three series of experiments were conducted corresponding to the different arrangements of displacement meters and phase-detection probe. The flow conditions are summarised in Table 1, together with a summary of earlier physical studies. For the data Series 1, the hydraulic jump flows were produced by a series of upstream gate openings h with the inflow Froude numbers Fr_1 from 3.8 to 10.0. The free-surface and two-phase properties were measured separately. For the data Series 2, the Froude number was set at $Fr_1 = 5.1$ and a range of gate openings were set to yield different Reynolds numbers from 2.1×10^4 to 1.63×10^5. The data Series 3 were set for three different Reynolds numbers with the same Froude number ($Fr_1 = 5.1$), and free-surface fluctuations and two-phase flow properties were recorded simultaneously at two longitudinal positions close to the jump toe, i.e. $(x\text{-}x_1)/d_1 = 4.15$ and 8.3.

Table 1. Experimental flow conditions

Ref.	Q (m^3/s)	h (m)	x_1 (m)	d_1 (m)	Fr_1	Re	Instrumentation
Murzyn and Chanson (2009)	0.020 to 0.042	0.018	0.75	0.018	5.1 to 11.2	4.0×10^4 to 8.3×10^4	1. Acoustic displacement meters (vertically placed) 2. Phase-detection probe
Chachereau and Chanson (2011)	0.020 to 0.065	0.036	1.50	0.039 to 0.044	1.35 to 5.1	3.9×10^4 to 1.3×10^5	1. Acoustic displacement meters (vertically placed) 2. Phase-detection probe
Zhang *et al.* (2013)	0.018 to 0.050	0.024	0.25 to 1.50	0.024 to 0.028	2.6 to 8.9	3.6×10^4 to 1.0×10^5	Phase-detection probes
Present study							
Series 1	0.0179	0.020	0.83	0.0206	3.8	3.5×10^4	1. Acoustic displacement meters (vertically placed) 2. Phase-detection probe
	0.0239			0.0209	5.1	4.8×10^4	
	0.0347			0.0206	7.5	6.8×10^4	
	0.0397			0.0208	8.5	8.0×10^4	
	0.0473			0.021	10.0	9.5×10^4	
	0.0352	0.030	1.25	0.0326	3.8	7.0×10^4	
	0.0461			0.0322	5.1	9.2×10^4	
	0.0709			0.033	7.5	1.41×10^5	
	0.0820	0.054	1.25	0.057	3.8	1.62×10^5	
Series 2	0.0160	0.012	0.5	0.012	5.1	2.1×10^4	Acoustic displacement meters (horizontally and vertically placed)
	0.0179	0.020	0.83	0.0206	3.8	3.5×10^4	
	0.0239			0.0209	5.1	4.8×10^4	
	0.0356			0.0209	7.5	6.8×10^4	
	0.0397			0.0208	8.5	8.0×10^4	
	0.0368	0.026	1.083	0.0277	5.1	7.4×10^4	
	0.0463	0.030	1.25	0.0322	5.1	9.2×10^4	
	0.0552	0.034	1.417	0.0363	5.1	1.10×10^5	
	0.0689	0.040	1.667	0.042	5.1	1.37×10^5	
	0.0815	0.045	1.875	0.047	5.1	1.63×10^5	
Series 3	0.0244	0.020	0.83	0.0206	5.1	4.7×10^4	Acoustic displacement meters together with phase-detection probe
	0.0463	0.030	1.25	0.0322	5.1	9.2×10^4	
	0.0701	0.040	1.25	0.0425	5.1	1.4×10^5	

Notes: Q: flow rate; h: sluice opening; x_1: longitudinal jump toe position; d_1: inflow depth; Fr_1: inflow Froude number; Re: Reynolds number.

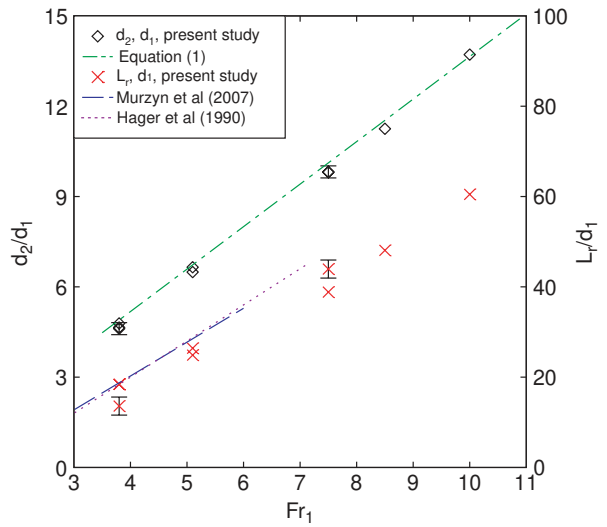

Figure 4. Conjugate depths and roller length of hydraulic jumps. Comparison with the solution of the momentum Equation (1), and empirical correlations of Hager *et al.* (1990) and Murzyn *et al.* (2007) for the roller length.

3. Free-surface characteristics

3.1 Free-surface profile

A hydraulic jump is characterised by a rapid increase in water elevation in the longitudinal direction together with a recirculation flow region (roller) downstream of the jump toe. The downstream depth d_2 data are presented in Figure 4, where the dimensionless depth d_2/d_1 is shown as function of the inflow Froude number Fr_1. The data compared well with the solution of the momentum principle (Equation (1)). The roller length L_r data are also presented in Figure 4. Herein L_r was defined as the distance over which the mean free-surface level increased monotonically (Murzyn *et al.* 2007, Murzyn and Chanson 2009). The data indicated an increasing roller length L_r/d_1 with increasing Froude number, and the data trend compared favourably with the empirical correlations of Murzyn *et al.* (2007) and Hager *et al.* (1990), but for a wider range of Froude numbers.

The longitudinal free-surface profiles were measured with acoustic displacement meters, located at six longitudinal positions along the centreline. Figure 5a shows the ratio of time-averaged water elevation to inflow depth η/d_1, the data presenting some shapes very similar to the visual observations through the sidewalls. The experimental data are plotted in Figure 5b. The free-surface elevation data showed a self-similar profile of the jump roller, which was best correlated by:

$$\frac{\eta - d_1}{d_2 - d_1} = \left(\frac{x - x_1}{L_r}\right)^{0.54} \quad (2)$$

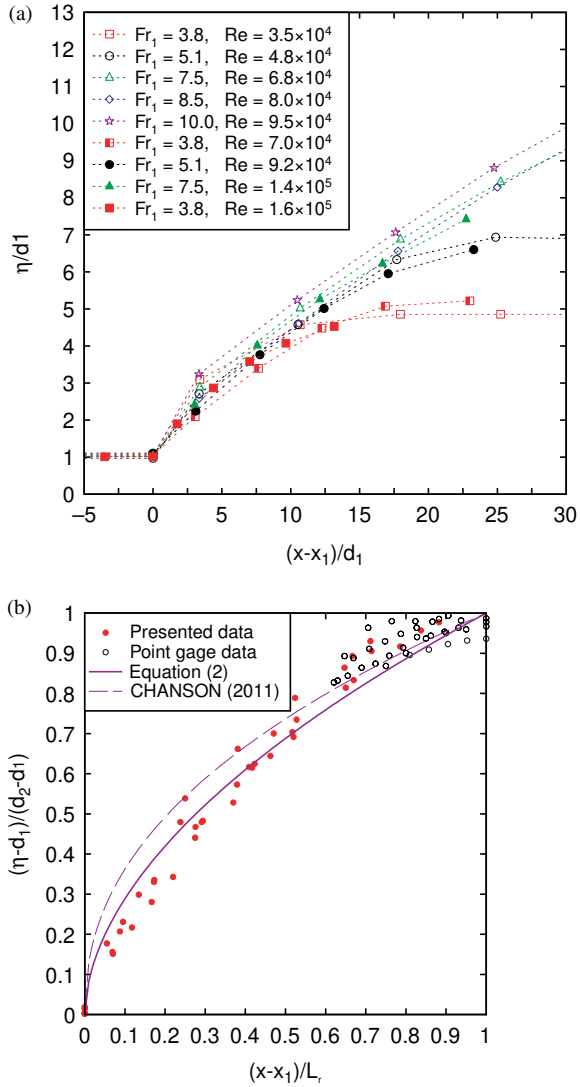

Figure 5. Time-averaged free-surface profiles – (a) dimensionless free-surface profiles at the centreline; (b) self-similar free-surface profiles within the roller length – comparison with Equation (2) and the correlation curve of Chanson (2011).

for $0 < x\text{-}x_1 < L_r$ within the range of experimental flow conditions (Table 1). The data are compared with Equation (2) in Figure 5B as well as with an earlier correlation proposed by Chanson (2011).

3.2 Free-surface fluctuations

3.2.1 Free-surface fluctuations and characteristic fluctuation frequencies

The instantaneous free-surface fluctuations were recorded continuously for a range of flow conditions (Table 1, series 1 and 2). A typical example is shown in Figure 6 together

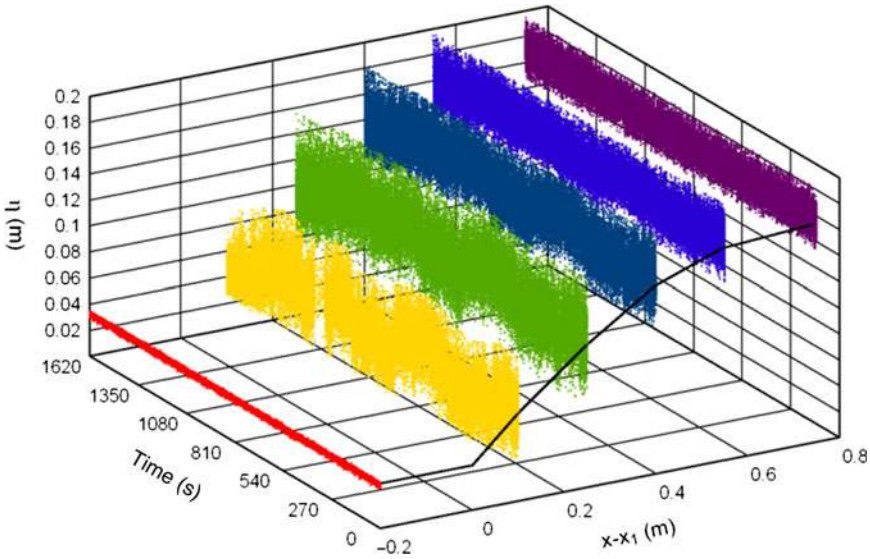

Figure 6. Instantaneous fluctuations of free-surface profile – flow conditions: $Q = 0.0352$ m^3/s, $d_1 = 0.0326$ m, $x_1 = 1.25$ m, $Fr_1 = 3.8$, $Re = 7.0 \times 10^4$.

with an outline of the time-averaged free-surface profile at $t = 0$. A relative steady inflow water level is shown upstream the jump toe ($x < x_1$), and the free-surface above the hydraulic jump roller fluctuated significantly with different amplitudes (Figure 6). The measurements showed that the maximum free-surface fluctuations were observed in the first half of the roller length. This is illustrated in Figure 7a presenting some typical longitudinal distributions of dimensionless standard deviations of water elevation η'/d_1as a functions of the dimensionless distance from the jump toe $(x\text{-}x_1)/L_r$. All the data showed large fluctuations in water elevation above the jump roller (i.e. $0 < (x\text{-}x_1)/L_r < 1$), while the water level fluctuations downstream of the roller remained larger than those recorded upstream of the jump toe. The maximum standard deviation of water elevation was consistently observed in the first half of the roller. The level of free-surface fluctuations tended to increase with increasing inflow Froude number, which was likely linked with the enhanced air entrapment at jump toe and air-water projections above the roller. The dimensionless maximum standard deviations η'_{max}/d_1 data are summarised against the inflow Froude number in Figure 7b where they are compared with the data of Mouaze *et al.* (2005), Kucukali and Chanson (2008) and Murzyn and Chanson (2009). All the physical data indicated a monotonic increase in maximum free-surface fluctuations with increasing Froude number for $2 < Fr_1 < 10$ (Figure 7b).

The frequencies of free-surface fluctuations were analysed based upon some displacement meter signal analyses. A fast Fourier transform yielded a power spectrum density (PSD) function, and the data showed some dominant characteristic frequency with a marked peak in energy density. Sometimes some secondary frequencies were seen as well. A typical PSD function is shown in Figure 8, in which the dominant and secondary free-surface fluctuation frequencies, denoted $F_{fs.dom}$ and $F_{fs.sec}$ respectively, are highlighted. Overall the dominant free-surface fluctuation frequencies $F_{fs.dom}$ on the channel centreline were typically between 1.2 and 3.5 Hz and the secondary frequencies $F_{fs.sec}$ between 0.5 and 1.2 Hz. The results were close between different longitudinal positions. The corresponding dimensionless data $F_{fs} \times d_1/V_1$ are shown as functions of the inflow Froude number in Figure 9. Herein two symbols connected by a dash line represent a range of frequencies when no unique frequency was observed (Figure 9). Both dimensionless dominant and secondary frequency data are shown in Figure 9, and the data highlighted a decreasing trend with increasing Froude number. The present data were best correlated by:

$$\frac{F_{fs,dom} \times d1}{V_1} = 0.163 \times \exp(-0.361 \times Fr_1) \quad (3a)$$

$$\frac{F_{fs,sec} \times d1}{V_1} = 0.021 \times \exp(-0.187 \times Fr_1) \quad (3b)$$

Equations (3a) and (3b) are compared with the experimental data in Figures 9a and 9b respectively. Chachereau and Chanson (2011) measured the free-surface fluctuations with a similar instrumentation. Their data provided a best fit correlation:

$$\frac{F_{fs} \times d1}{V_1} = 0.143 \times \exp(-0.27 \times Fr_1) \quad (4)$$

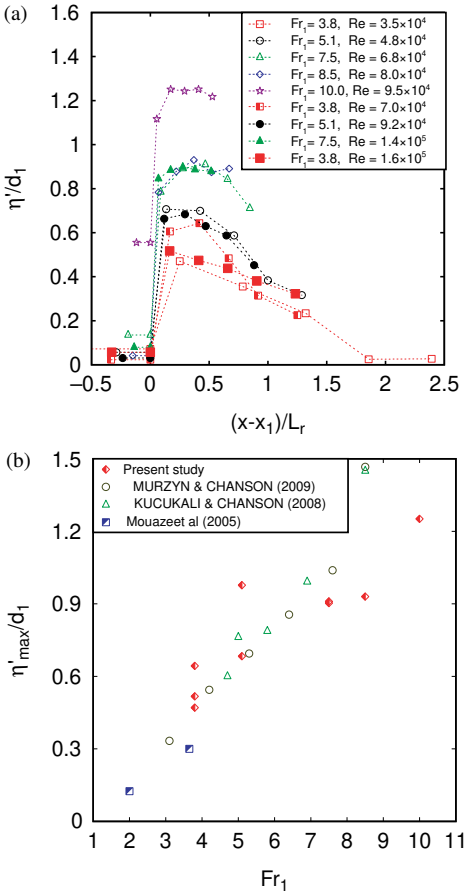

Figure 7. Free-surface fluctuations – (a) dimensionless standard deviation of free-surface profile fluctuations; (b) maximum free-surface fluctuations as a function of inflow Froude number – Comparison with Mouaze *et al.* (2005), Kucukali and Chanson (2008) and Murzyn and Chanson (2009).

which is plotted in Figure 9a for comparison. Altogether Equations (3a) and (4) showed a comparable trend for a wide range of Froude numbers ($2.4 < Fr_1 < 10$) (Figure 9a).

The secondary characteristic frequency data showed quantitative results comparable to previous observations, namely the frequency of longitudinal jump toe oscillations F_{toe} and frequency of downstream ejection of large scale vortices F_{ej} (Zhang *et al.* 2013). In a stationary hydraulic jump, the jump toe oscillated around its mean longitudinal position x_1, and large scale vortices were generated at and advected downstream of the jump toe. Zhang *et al.* (2013) showed some relationships between the oscillation frequency F_{toe} and vortices advection frequency F_{ej}, and the inflow Froude number:

$$\frac{F_{toe} \times d1}{V_1} = 0.054 \times \exp(-0.33 \times Fr_1) \quad (5)$$

$$\frac{F_{ej} \times d1}{V_1} = 0.034 \times \exp(-0.26 \times Fr_1) \quad (6)$$

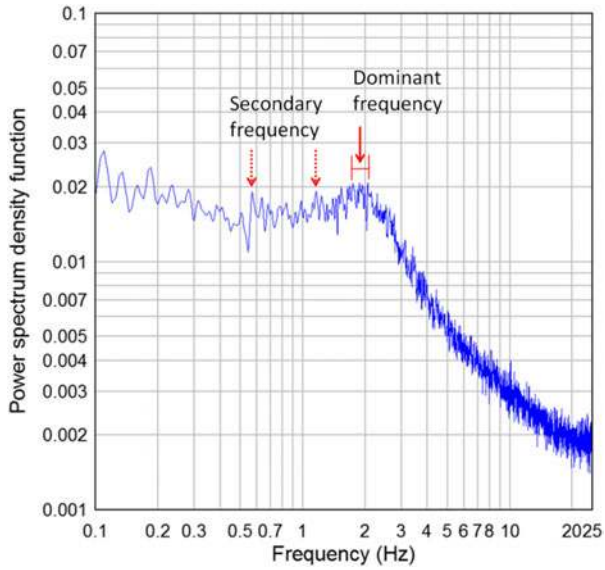

Figure 8. Power spectrum density function of acoustic displacement meter signals – flow conditions: $Q = 0.0461$ m^3/s, $d_1 = 0.0322$ m, $x_1 = 1.25$ m, x-$x_1 = 0.4$ m, $Fr_1 = 5.1$, $Re = 9.2 \times 10^4$.

Equations (5) and (6) are compared with Equation (3b) in Figure 9b, showing a close agreement. It is believed that the oscillation of jump toe and the generation and advection of large scale vortices in the roller are linked (Long *et al.* 1991, Mossa and Tolve 1998, Chanson 2010). The close agreement between all the data (Figure 9b) may suggest some coupling between the longitudinal jump toe oscillation, the ejection of large scale vortices and the free-surface fluctuations.

For some experiments performed with the same Froude number ($Fr_1 = 5.1$) and a range of Reynolds numbers ($2.1 \times 10^4 < Re < 1.63 \times 10^5$), the data indicated little differences in terms of the dimensionless characteristic frequencies of free-surface fluctuations. The frequency data ranges were close to the data shown in Figure 9 and yielded: $1.8 < F_{fs.dom} < 3.7$ Hz and $0.4 < F_{fs.sec} < 1.7$ Hz. Simply the inflow Froude number was the dominant factor affecting the free-surface fluctuation frequencies, rather than the Reynolds number.

3.2.2 *Wave celerity at the roller free-surface*

Visually the fluctuations at the free-surface appeared to propagate above the roller in the downstream direction. Based upon a cross-correlation analysis of displacement meter signals, the wave celerity at the free-surface was calculated as $U = \Delta x/\Delta t$, where Δx is the longitudinal distance between two adjacent sensors along the centreline, and Δt is the time lag for which the cross-correlation function is maximum. The data are presented in Figure 10 in terms of the ratio of wave celerity to

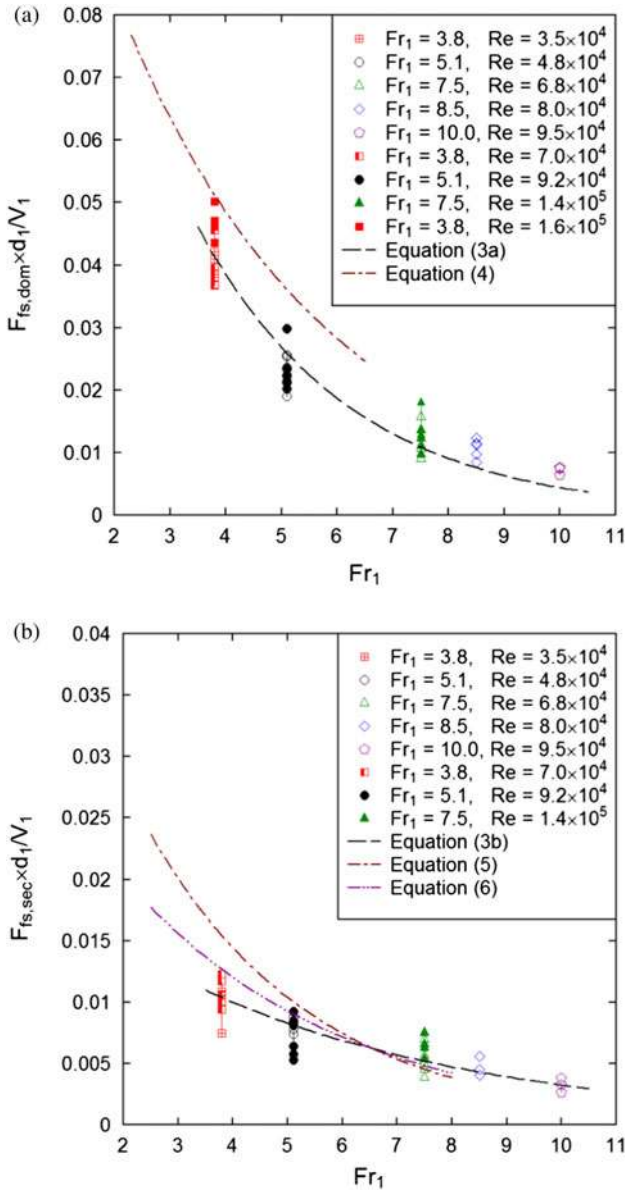

Figure 9. Dimensionless characteristic free-surface fluctuation frequencies as functions of inflow Froude number – (a) dominant frequencies; (b) secondary frequencies.

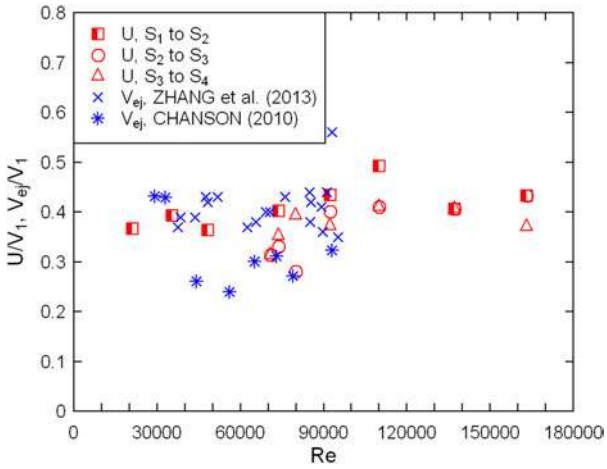

Figure 10. Ratio of wave celerity in free-surface to inflow velocity – Comparison with the average advection velocity of large scale vortices in the roller from Zhang *et al.* (2013) and Chanson (2010).

inflow velocity U/V_1. For a given experiment, the results were close between different sensors on the channel centreline, implying that the free-surface fluctuations propagated at a nearly constant celerity independently of the longitudinal location. Overall the ratio U/V_1 was nearly independent of the Reynolds number, with an average value $U/V_1 = 0.39$ (Figure 10). Figure 10 includes also the average advection velocities of large scale vortices in the roller V_{ej}/V_1 observed by Chanson (2010) and Zhang *et al.* (2013). Comparable results are shown, with mean values of 0.32 and 0.41 respectively. Altogether the experimental data implied that the propagation of free-surface fluctuations at the roller surface was closely linked to the advection of large scale vortices in the shear layer.

3.3 *Longitudinal change in jump toe position*

The hydraulic jump location shifted around a position x_1 in both fast and slow manners. The characteristic frequency of the fast longitudinal motion of jump toe position was typically $0.003 < F_{toe} \times d_1/V_1 < 0.025$, corresponding to dimensional frequencies between 0.7 and 1.3 Hz (Zhang *et al.* 2013). The slow change in jump position had a frequency typically significantly lower than 0.1 Hz, and limited data were reported to date. In the present study, both the fast and slow fluctuations in jump toe position were investigated. Some long-term change of jump position was recorded with a video camera, while the rapid jump toe oscillations were detected with a horizontal displacement meter from upstream, as illustrated in Figure 3 (sensor S_o).

3.3.1 *Long-term change in longitudinal roller position*

Video observations for up to 160 min. were conducted for a hydraulic jump with $Fr_1 = 5.1$ and $Re = 4.8 \times 10^4$. Some typical video frames are presented in Figure 11. The relative jump toe position x-x_1 was recorded every second, and some typical smoothed data are shown in Figure 12. The data highlighted some temporary changes of jump toe position ranging from -0.28 m to +0.12 m, with the largest movements being mostly in the form of upstream shifts (x-$x_1 < 0$). The jump toe tended to stay at the remote positions for 120 to 400 s before returning to its mean position. The displacements were larger than, and their

Figure 11. Video frames of hydraulic jump toe position in side view.

periods were drastically longer than, those for the rapid jump toe oscillations. In Figure 12, about 36 major shifts in jump toe positions were recorded during 160 min. corresponding to an average frequency around 0.004 Hz. It is thought that the relative long-term behaviour might be linked with the hydraulic jump minimising its energy. For example, an upstream movement of jump roller tended to decrease the downstream water level to achieve lower potential energy. At the same time, it decreased slightly the inflow depth because of a lesser developed boundary layer at the channel bed, thus corresponding to a temporary increase in inflow Froude number, which tended to increase the ratio of conjugate depths d_2/d_1 according to momentum considerations (Equation (1)).

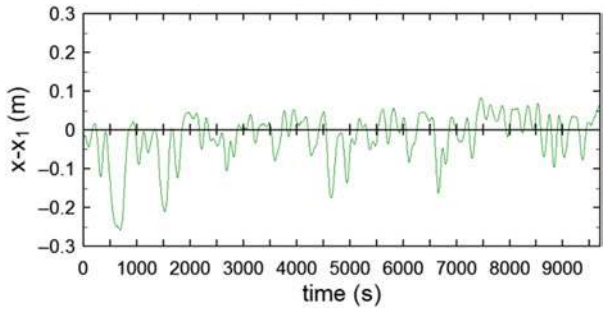

Figure 12. Time-variation of the instantaneous relative jump toe position.

3.3.2 *Longitudinal jump toe oscillations*

The horizontally placed displacement meter (sensor S_0 in Figure 3) detected the longitudinal position of roller front which moved together with the jump toe. The characteristic oscillation frequencies were deduced from the signal analysis and the dominant and secondary frequencies were denoted $F_{toe.dom}$ and $F_{toe.sec}$ respectively. The dimensionless frequency data are shown in Figure 13a as functions of the inflow Froude number and in Figure 13b against the Reynolds number. Some visual observations during previous studies are also included for comparison. In Figure 13a, the data showed that the dimensionless frequencies of horizontal jump fluctuations were close to the visual observations, but for those of Zhang *et al.* (2013) and Chachereau and Chanson (2011) at low Froude numbers ($Fr_1 < 4.4$). Some results obtained with an identical Froude number presented higher dominant frequencies at larger Reynolds numbers, though the previous observations only focused on Reynolds numbers less than 1.1×10^5 (Figure 13b). A reason for the discrepancy at low Froude and Reynolds numbers might be linked with the difficulty to aim the displacement meter at the jump front close to the jump toe for small hydraulic jumps.

The approximate frequency ranges are listed in Table 2. The dominant characteristic frequencies of jump toe oscillation $F_{toe.dom}$ were shown within a similar range to the secondary characteristic frequencies $F_{fs.sec}$ observed for the free-surface fluctuations, while the secondary jump toe oscillation frequencies $F_{toe.sec}$ were in a range corresponding to the dominant free-surface fluctuation frequencies $F_{fs.dom}$. The findings implied that the vertical free-surface fluctuations and horizontal roller

Table 2. Characteristic frequencyranges of free-surface fluctuations and jump toe oscillations measured with acoustic displacement meters at channel centreline (Present study)

Parameter	Dominant frequency (Hz)	Secondary frequency (Hz)
Free-surface fluctuation (F_{fs})	1.2–3.5	0.5–1.2
Jump toe oscillation (F_{toe})	0.5–1.3	0.8–2.6

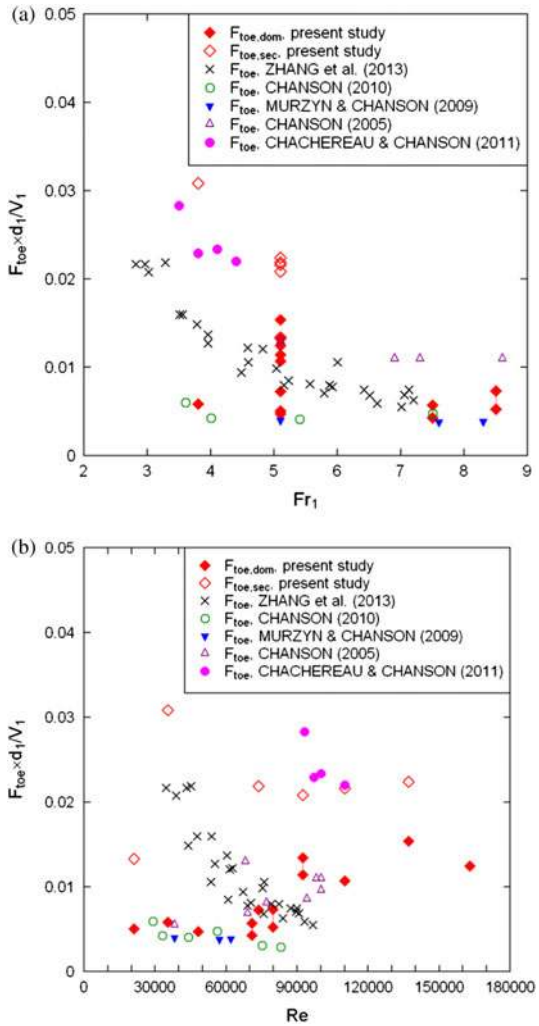

Figure 13. Dimensionless characteristic frequencies of jump toe oscillations – Comparison with visual observation results of Zhang *et al.* (2013), Chanson (2005, 2010), Murzyn and Chanson (2009) and Chachereau and Chanson (2011) – (a) dimensionless jump toe oscillation frequencies as functions of inflow Froude number; (b) dimensionless jump toe oscillation frequencies as functions of Reynolds number.

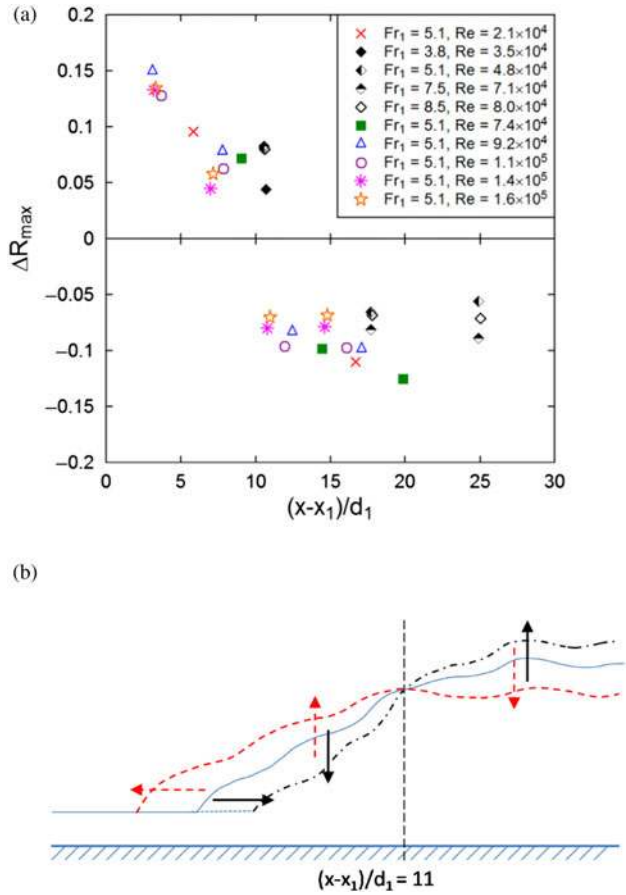

Figure 14. Simultaneous free-surface deformations in horizontal and vertical directions – (a) relative maximum cross-correlation coefficient between the signals of horizontal and vertical displacement meters; (b) sketch of surface deformation patterns.

oscillations were not independent processes. The two motions had different inherent characteristic frequencies, although they interacted with each other, the influence being reflected by some secondary frequencies.

3.4 Simultaneous vertical and horizontal free-surface motions

Some cross-correlation analyses were performed between the horizontal and vertical displacement meter signals. The relative maximum or minimum correlation coefficients with zero time lag ($\tau = 0$) characterised some simultaneous fluctuating motions of the roller surface in the two directions. For a given set of flow conditions, the horizontal jump front position data was correlated to the water elevation data measured at different longitudinal locations on the centreline. Figure 14a presents the peak correlation coefficients at the corresponding positions of the vertical sensors. For all data, the relative maximum correlation coefficients ΔR_{max} were positive for $(x\text{-}x_1)/d_1 < 11$, and the relative minimum were less than zero for $(x\text{-}x_1)/d_1 > 11$ (Figure 14a). The positive peak indicated that the local free-surface elevation increased when the jump toe moved upstream and decreased when the jump toe moved downstream. The opposite trends were indicated by the negative peak value. That is, at the relative close positions to the jump toe, the free-surface moved as a whole, hence increase/decrease in both horizontal and vertical directions were shown synchronously. At further downstream positions, the water level was simply decided by conservation of mass and momentum. These relative motions of the jump roller surface are sketched in Figure 14b, highlighting the free-surface deformation patterns.

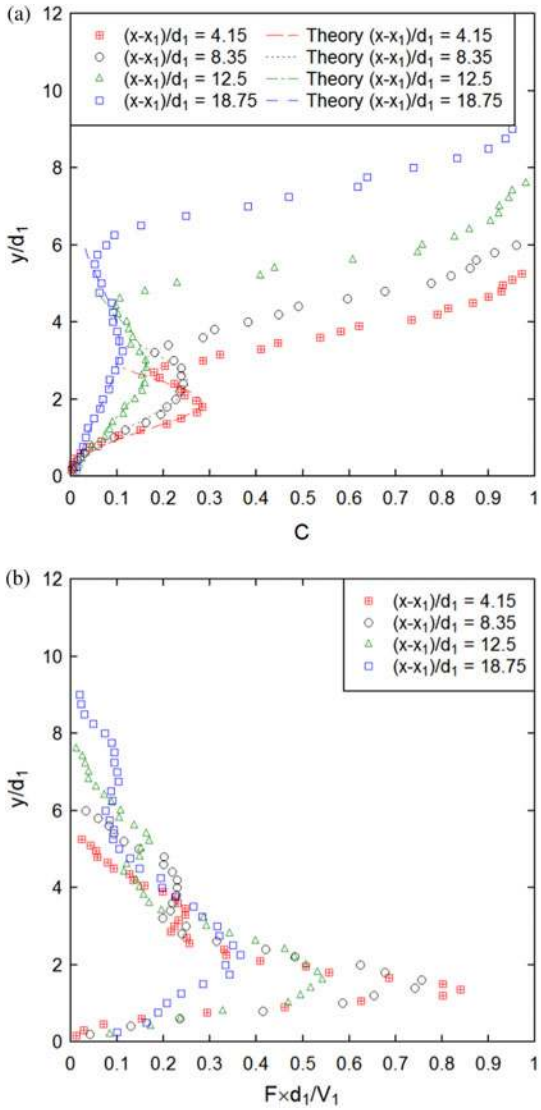

Figure 15. Vertical distributions of basic air-water flow properties – Flow conditions: $Q = 0.0347$ m^3/s, $d_1 = 0.0206$ m, $x_1 = 0.83$ m, $Fr_1 = 7.5$, $Re = 6.8 \times 10^4$ – (a) void fraction; (b) dimensionless bubble count rate.

4. Air-water flow properties

4.1 Void fraction and bubble count rate

The air-water flow properties of hydraulic jumps were measured with an intrusive conductivity probe detecting the air-water interfaces. The instantaneous void fraction c was recorded by the raw signal, and the time-averaged void fraction C and bubble count rate F were derived after data processing. Figure 15 presents some vertical distributions of void fraction and dimensionless bubble count rate along the roller centreline. Note that all the data shown in Figure 15 were time-averaged measurements. Leandro *et al.* (2012) performed some simultaneous measurements of complete time series of vertical void fraction profiles, emphasising the rapid fluctuations in instantaneous two-phase flow properties. Herein the vertical distributions highlighted two flow regions, namely a shear layer between the channel bed and roughly the elevation of local minimum void fraction $y*$, and a recirculation region above. At the impingement point, highly-aerated vortices were generated and advected downstream in the shear region. In the shear layer, some local maxima in void fraction C_{max} and bubble count rate F_{max} were observed at different elevations, y_{Cmax} and y_{Fmax} respectively. In the recirculation region, the void fraction increased monotonically from the local minimum $C*$ to unity, whereas the bubble count rate showed a secondary peak and decreased to zero (Figure 15). This flow region was characterised by some flow recirculation motion, together with aeration and deaeration at the upper free-surface.

In the shear region, the void fraction distribution followed an analytical solution of the advective diffusion equation for air bubbles (Chanson 1995, 2010):

$$C = C_{max} \times \exp\left[-\frac{1}{4 \times D^{\#}} \times \frac{\left((y - y_{C_{max}})/d_1\right)^2}{\left((x - x_1)/d_1\right)}\right] \quad (7)$$

where $D^{\#}$ is the dimensionless diffusivity: $D^{\#} = D_t/(V_1 \times d_1)$ with D_t being the air bubble diffusivity. Equation (7) is compared with experimental data in Figure 15a. The maximum void fraction C_{max} decreased along the longitudinal direction in the roller for a given set of flow conditions. The data followed an exponential trend:

$$C_{max} = A \times \exp\left[-B \times \left(\frac{x - x_1}{d_1}\right)\right] \quad (8)$$

where A and B are the best-fitted coefficients functions of the flow conditions. In the present study, the coefficients A and B were linked to the inflow Froude number, but almost independent of the Reynolds number:

$$A = 0.436 + 0.014 \times Fr_1 \quad (9a)$$

$$B = 0.911 \times \exp(-0.335 \times Fr_1) \quad (9b)$$

Consequently, the maximum void fraction C_{max} was a function of the longitudinal position and inflow Froude number:

$$C_{max} = (0.436 + 0.014 \times Fr_1) \times \exp\left\{-[0.911 \times \exp(-0.335 \times Fr_1)] \times \left(\frac{x - x_1}{d_1}\right)\right\} \quad (10)$$

Similarly, the present data indicated a longitudinal decay in maximum bubble count rate with increasing distance from

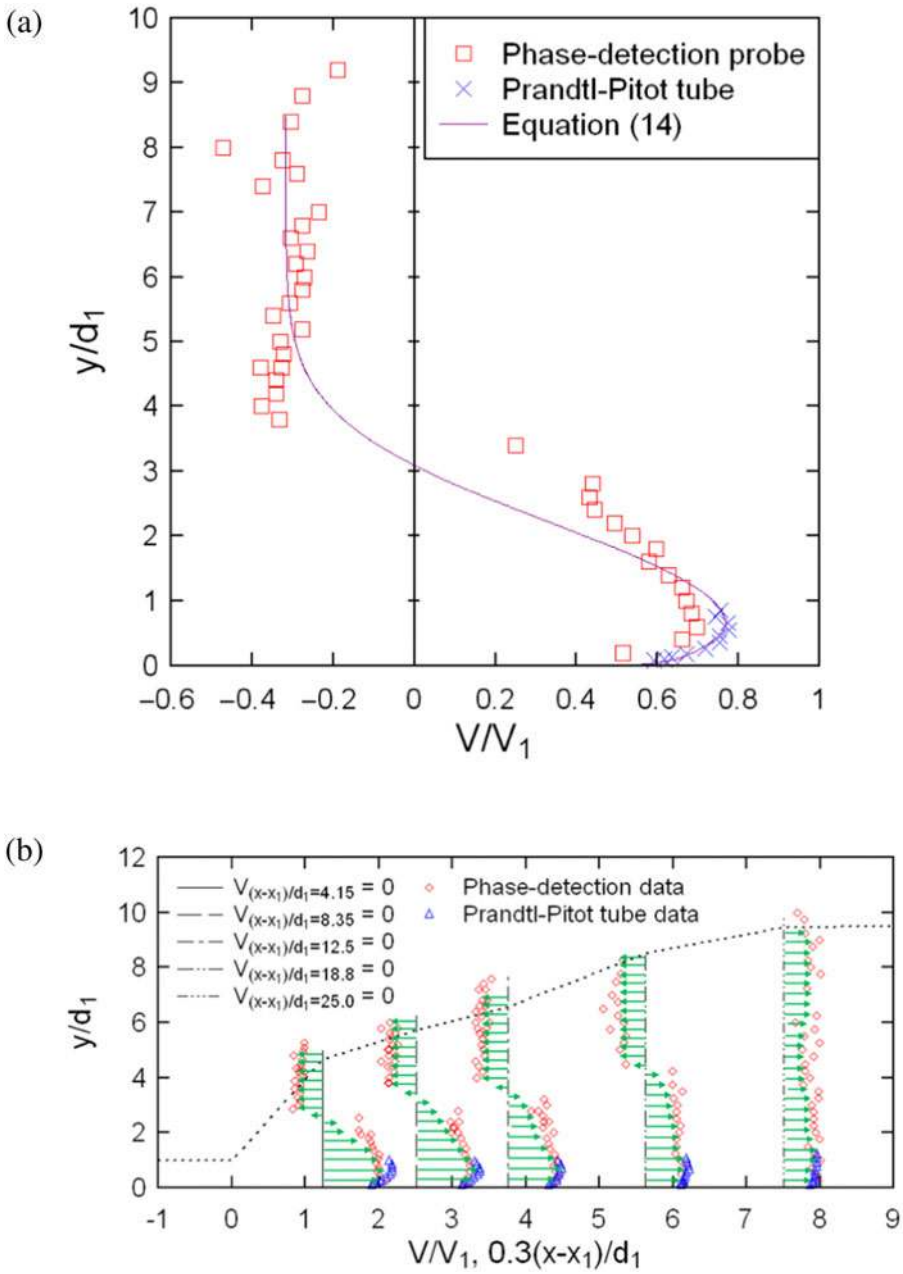

Figure 16. Interfacial velocity distribution together with Prandtl-Pitot tube data – (a) typical interfacial velocity profile; (b) velocity distribution through the jump roller.

the jump toe. The data were best correlated as:

$$\frac{F_{max} \times d_1}{V_1} = \left(0.343 + 0.131 \times \frac{Re}{10^4}\right) \times \exp\left\{-[0.511 \times \exp(-0.29 \times Fr_1)] \times \left(\frac{x - x_1}{d_1}\right)\right\} \quad (11)$$

Equations (10) and (11) indicated that the quantitative levels of the maxima in void fraction and bubble count rate respectively were functions of the Froude number for void fraction C_{max} and of the Reynolds number for dimensionless bubble count rate F_{max}, whereas the decay rates along the roller were mostly affected by the Froude number in each case. The finding implied that the amount of entrapped air and the number of air bubbles were related to different physical processes: the former was likely linked to the inertia force and the latter to the turbulence shear force.

The elevations of maximum void fraction y_{Cmax} and maximum bubble count rate y_{Fmax} increased with increasing distance from the jump toe. The data were best fitted by

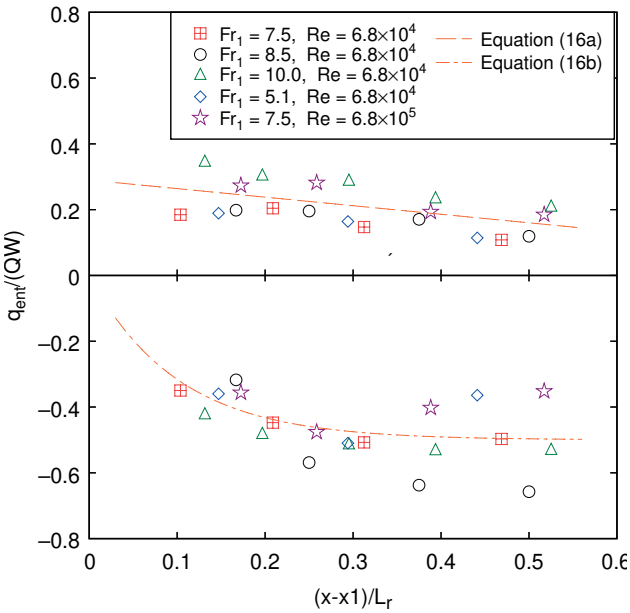

Figure 17. Entrapped air flux in jump roller.

some linear regressions:

$$\frac{y_{C_{max}}}{d_1} = 1.48 + 0.084 \times \frac{x - x_1}{d_1} \quad (12)$$

$$\frac{y_{F_{max}}}{d_1} = 1.20 + 0.045 \times \frac{x - x_1}{d_1} \quad (13)$$

4.2 *Interfacial velocity and entrapped air flux*

The interfacial velocity was deduced from a cross-correlation analysis of the dual-tip phase-detection probe signals in the aerated flow region. A Prandtl-Pitot tube was used to measure the clear-water velocity in the lower shear layer where the void fraction was typically less than 0.05 and the accuracy of phase-detection probe was limited. A typical velocity profile is shown in Figure 16a. Altogether, the velocity data exhibited some profiles similar to with a wall jet flow (Rajaratnam 1965, Chanson 2010):

$$\frac{V}{V_{max}} = \left(\frac{y}{y_{Vmax}}\right)^{1/N} \quad \text{for} \quad \frac{y}{y_{Vmax}} < 1 \quad (14a)$$

$$\frac{V - V_{recirc}}{V_{max} - V_{recirc}} = \exp\left(-\frac{1}{2} \times \left(1.765 \times \frac{y - y_{Vmax}}{y - y_{0.5}}\right)^2\right) \quad \text{for} \quad \frac{y}{y_{Vmax}} > 1 \quad (14b)$$

where N is a constant, V_{max} is the maximum velocity measured at $y = y_{Vmax}$, V_{recirc} is the recirculation velocity and $y_{0.5}$is the elevation where $V = 0.5 \times V_{max}$. Herein V_{recirc} was found nearly uniform at a given longitudinal position across the recirculation region, while $N = 10$ typically (Figure 16a). Although the cross-correlation analysis failed to provide meaningful results in the region where the interfacial velocity was about zero, some statistical analysis of instantaneous time lag in the raw probe signals supported the continuous velocity profile prediction by showing small average velocity close to $y(V = 0)$. Note that the elevation $y(V = 0)$ differed slightly from the characteristic elevation $y*$. An example of the longitudinal variations in vertical velocity distributions is shown in Figure 16b, together with the time-averaged free-surface profile. The maximum velocity was observed to the channel bed and its magnitude decreased with increasing distance from the jump toe. Some recirculation motion was shown clearly in the recirculation region within the upper region of the jump roller.

Based upon the void fraction and velocity measurements, the entrapped air flux in the jump roller was derived from the equation of conservation of mass for the air phase:

$$q_{ent} = \int_{y=0}^{y_{90}} C \times V \times dy \quad (15a)$$

where y_{90} is the characteristic distance from the bed where $C = 0.90$. For the experimental flows with some distinct flow recirculation in the upper roller region, the air flux q_{ent} was calculated in two flow regions: (a) for $0 < y < y(V = 0)$ and (b) for $y(V = 0) < y < y_{90}$, where $y_{90} = y(C = 0.9)$ was considered as an upper free-surface elevation estimate:

$$q_{ent}^{(a)} = \int_{y=0}^{y(V=0)} C \times V \times dy > 0 \quad (15b)$$

$$q_{ent}^{(b)} = \int_{y=y(V=0)}^{y_{90}} C \times V \times dy < 0 \quad (15c)$$

Equation (15b) characterised the air flow rate entrained in the shear region, while Equation (15c) described the recirculation air flux in the upper region (b), assuming an uniform recirculation velocity. The longitudinal distributions of entrained and recirculation air fluxes are plotted in Figure 17, together with the best fit correlation functions:

$$\frac{q_{ent}^{(a)}}{(Q/W)} = 0.29 - 0.26 \times \frac{x - x_1}{L_r} \quad \text{for} \quad 0 < y < y(V = 0) \quad (16a)$$

$$\frac{q_{ent}^{(b)}}{(Q/W)} = -0.5 \times \left(1 - \exp\left(-10 \times \frac{x - x_1}{L_r}\right)\right) \quad \text{for} \quad y(V = 0) < y < y_{90} \quad (16b)$$

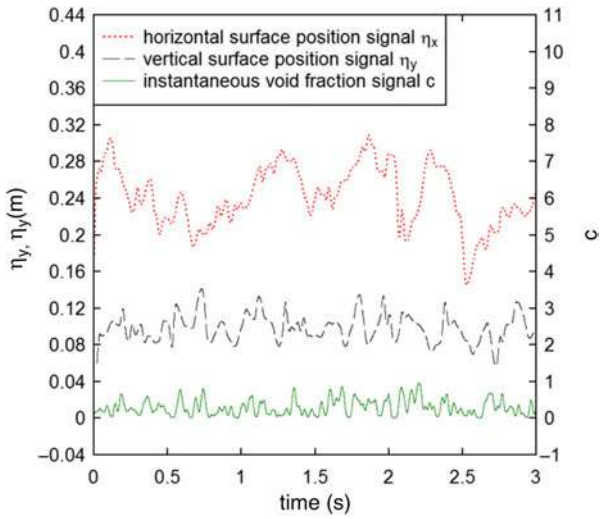

Figure 18. Post-processed signals for simultaneous free-surface and void fraction measurements – flow conditions: $Q = 0.0463$ m^{3}s, $d_1 = 0.0322$ m, $x_1 = 1.25$ m, $Fr_1 = 5.1$, $Re = 9.2 \times 10^4$, x-$x_1 = 0.125$ m, $y = 0.040$ m.

The positive air flux in the shear region ($0 < y < y(V = 0)$) was shown to decrease with increasing distance from the jump toe, as the air bubbles were diffused and dispersed by turbulent shear. Air bubbles were observed to be driven into the upper recirculation region by buoyancy as they were advected in the streamwise advection. In the recirculation region ($y(V = 0) < y < y_{90}$), the air flux was negative, and its magnitude increased rapidly within $0 < x$-$x_1 < 0.3 \times L_r$, and sightly increased over the rest roller length. The qualitative trend and quantitative data suggested some significant air entrapment at the jump toe. Further downstream, the aeration rate still appeared to be higher than the de-aeration rate, because the air flux in the recirculation region was larger than that in the shear layer: the finding implied that the air entrapment flux was not the only source of the recirculating negative flux.

Overall the data suggested that the flux of air entrapment at jump toe was roughly 30% of the water discharge for $5.1 < Fr_1 < 10$ (Figure 17) and all entrapped air was advected into the shear layer. In most cases, the total absolute air flux $|q_{ent}| = |q_{ent}^{(a)}| + |q_{ent}^{(b)}|$ reached a maximum at x-$x_1 = 0.3 \times L_r$, as additional aeration took place through the free-surface of the roller.

5. Coupling between free-surface and air-water flow property fluctuations

Simultaneous measurements of instantaneous void fraction c and relative roller surface locations, η_x in the horizontal direction and η_y in the vertical direction, were conducted as sketched in Figure 3b.The phase-detection probe and acoustic displacement meters were sampled synchronously at 5 kHz for 180 s at each phase-detection

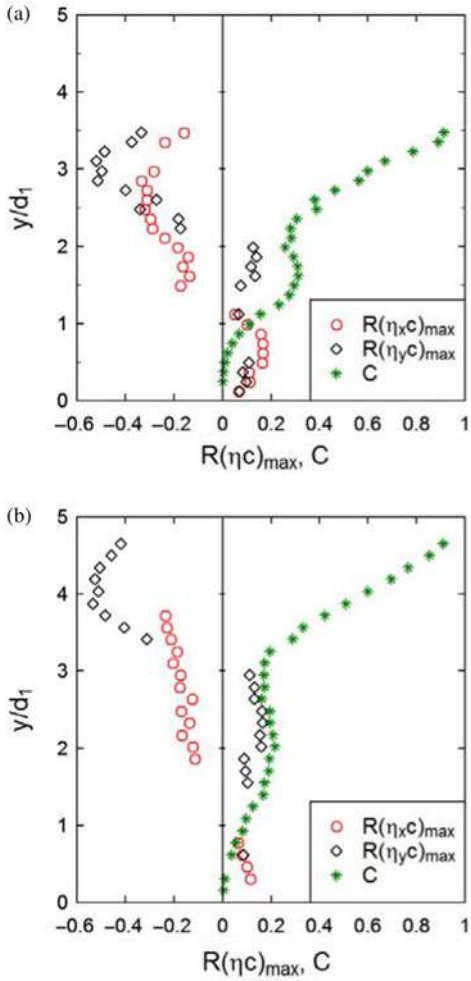

Figure 19. Maximum cross-correlation coefficients and time-averaged void fraction distributions – flow conditions: $Q = 0.0463$ m^{3}s, $d_1 = 0.0322$ m, $x_1 = 1.25$ m, $Fr_1 = 5.1$, $Re = 9.2 \times 10^4$ – (a) x-$x_1 = 0.125$ m; (b) x-$x_1 = 0.25$ m.

probe location (x, y).The processed signals were filtered with a low-pass band (0–25 Hz) to eliminate high-frequency component with a period less than the response time of the displacement meter (Murzyn and Chanson 2009). The low-pass filtered signals were smoothed and Figure 18 shows a typical example. A cross-correlation function was calculated between the data of horizontal jump front position η_x and instantaneous void fraction c, as well as between those of water elevation η_y and instantaneous void fraction, yielding the corresponding cross-correlation correlation functions $R(\eta_x c)$ and $R(\eta_y c)$.

The measurements were performed at longitudinal positions close to the jump toe: $(x$-$x_1)/d_1 = 4$ and 8. For a constant Froude number $Fr_1 = 5.1$ and Reynolds numbers from $4.7 \times 10^4$to 1.4×10^5, the measurements and corresponding calculations were performed for a range of phase-detection elevations $0 < y/d_1 < y_{90}/d_1$. Maximum (or minimum) correlation coefficients $R(\eta_x$-$c)_{max}$ and $R(\eta_y c)_{max}$ were observed at most vertical

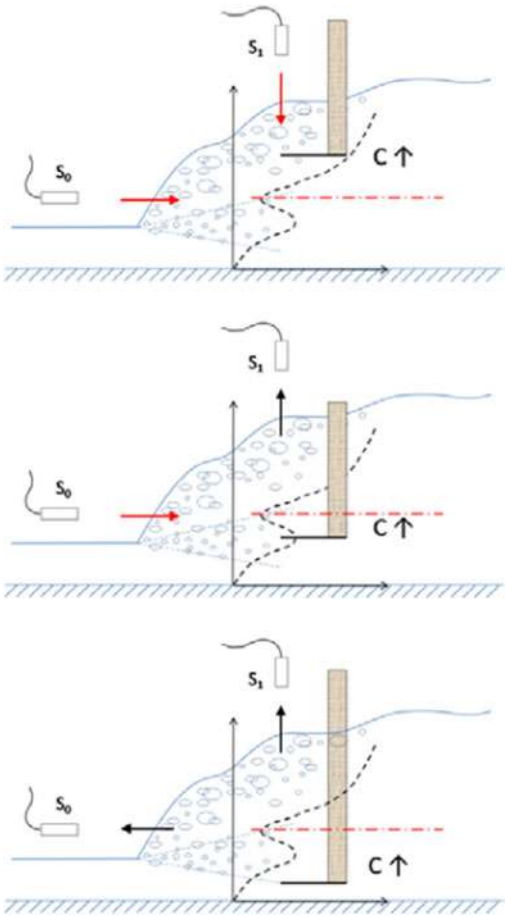

Figure 20. Sketches of free-surface deformations – (top) void fraction measured in recirculation region; (middle) void fraction measured in middle shear layer; (bottom) void fraction measured in lower shear layer.

elevations, giving some measure of the relative fluctuations in free-surface position and void fraction. Figure 19 presents some typical vertical distributions of maximum cross-correlation coefficients at two longitudinal positions in the first half roller, together with the time-averaged void fraction C distribution.

At a given cross-section, positive maximum correlation coefficients were shown in terms of $R(\eta_x c)$ and $R(\eta_y c)$ in the lower shear layer: i.e., $0 < y < y(C = 0.1)$. The positive maxima were seen at about zero time lag ($\tau = 0$), indicating some increasing distance η_x and η_y with increasing local instantaneous void fraction. The air bubbles in this region were mostly entrapped air advected downstream of the jump toe. That is, when the diffused air was detected within $0 < y < y(C = 0.1)$, the jump roller moved upstream and both water elevation and relative jump front position increased as sketched in Figure 20C. Similarly, negative maxima were show in terms of both $R(\eta_x c)$ and $R(\eta_y c)$ in the recirculation region (y > y*) (Figure 19). Note that the negative peak $R(\eta_x c)_{max}$ was seen with a negative time lag $\tau < 0$, while the peak $R(\eta_y c)_{max}$ was observed for $\tau = 0$. The data indicated that the instantaneous void fraction increased in the recirculation region when the local water level decreased, followed by a downstream movement of the jump toe (Figure 20 (top)). Different physical processes might be involved implied; for example, a negative $R(\eta_y c)_{max}$ next to the free-surface might be the result of the probe tip being exposed to air as the water surface elevation dropped and being re-submerged as the water surface shifted upwards.

In the main air bubble advection zone of shear layer, i.e. $y(C = 0.1) < y < y*$, the data indicated maximum cross-correlation coefficients with opposite signs: namely $R(\eta_x c)_{max} < 0$ and $R(\eta_y c)_{max} > 0$. The observations corresponded to an increasing void fraction together with a downstream jump toe motion and an increasing free-surface elevation above. The free-surface motions might reflect the flow bulking associated with the air entrapment at the jump toe, detachment and downstream advection of large aerated coherent structures (Figure 20 (middle)), while the fluctuations in void fraction might correspond to the air entrapped and advected in the large scale coherent structures. Thus the results implied a coupling between the instantaneous free-surface deformations and air-water flow properties linked with the convection of highly-aerated large-scale vortices. Figures 20 (top) and 20 (bottom) present some sketches of flow patterns and free-surface deformations close to those shown in Figure 14b for $(x\text{-}x_1)/d_1 < 11$. On the other hand, the trend illustrated in Figure 20 (middle) was not revealed by the direct correlation between the free-surface fluctuations (Section 3.4).

6. Conclusion

The physical modelling of hydraulic jumps with partially developed inflow conditions was investigated in a relatively large sized facility. Abroad range of Froude numbers ($3.8 < Fr_1 < 10.0$) and Reynolds numbers ($2.1 \times 10^4 < Re < 1.6 \times 10^5$) were tested. The free-surface fluctuations were measured non-intrusively with acoustic displacement meters, and the air-water flow properties were measured using an intrusive phase-detection probe.

The time-averaged free-surface profile was well defined on the channel centreline, presenting some self-similarity within the length of roller. The largest free-surface fluctuations were observed in the first half roller, and the maximum fluctuations increased with inflow Froude number. The characteristic free-surface fluctuation frequencies encompassed both dominant and secondary frequencies. The dimensionless frequencies decreased exponentially with increasing Froude number. The longitudinal oscillation of the jump roller position exhibited some dominant and secondary characteristic frequencies. The frequency ranges implied some coupling

between the vertical and horizontal motions of the roller surface, supported by some cross-correlation analysis of the corresponding signals. The frequency of vertical free-surface fluctuations was mostly affected by the Froude number, while the horizontal jump toe oscillations were linked with both Froude and Reynolds numbers within the experimental flow conditions. The type of free-surface deformation was different at different longitudinal positions. The wave propagation celerity at the roller free-surface was shown to be close to the advection speed of large vortices in the roller. Some slow changes in the roller position were also observed with large jump toe displacement and long shifting time.

The distributions of void fraction, bubble count rate and interfacial velocity were measured in the hydraulic jump roller. Maximum void fraction and bubble count rate were observed in the developing shear layer, but at different elevations. The interfacial velocity profiles showed some agreement with a wall jet solution. The entrapped air flux was estimated based upon the integration of the void fraction and velocity data. The results implied some aeration and de-aeration processes in different flow region. Simultaneous measurements of vertical/horizontal free-surface fluctuations and instantaneous void fraction highlighted the coupling between the free-surface fluctuations and local air-water flow properties. The results suggested some non-constant free-surface deformation patterns linked with variations in void fraction at different locations within the roller. As the roller moved upstream, the air entrainment increased in the lower shear layer but decreased in the recirculation region. When more entrapped air was detected in the bulk of the shear layer, the jump toe tended to move downstream, together with some flow bulking of the roller surface.

The findings provide a range of information on both turbulent free-surface fluctuations and two-phase flow properties. New data in terms fluctuation frequencies, surface deformation patterns and air entrapment estimation were presented, and the study of the interaction between turbulence development and air entrainment brought further insight to this complex flow. The findings may have implication into the design of water systems in which hydraulic jumps may occur.

Acknowledgements

The authors thank Jason van der Gevel and Stewart Matthews (The University of Queensland) for their technical assistance in laboratory work.

Funding

The financial support of the Australian Research Council [Grant numbers DPDP0878922 & DP120100481] is acknowledged.

References

Bélanger, J.B., 1841. *Notes sur l'hydraulique [Notes on hydraulic engineering]*. Paris, France: Ecole Royale des Ponts et Chaussées. session 1841-1842 [in French].

Chachereau, Y. and Chanson, H., 2011. Free-surface fluctuations and turbulence in hydraulic jumps. *Experimental Thermal and Fluid Science*, 35 (6), 896–909.

Chanson, H., 1995. Air entrainment in two-dimensional turbulent shear flows with partially developed inflow conditions. *Journal of Multiphase Flow*, 21 (6), 1107–1121.

Chanson, H., 2007a. Bubbly flow structure in hydraulic jump. *European Journal of Mechanics - B/Fluids*, 26 (3), 367–384.

Chanson, H., 2007b. Dynamic similarity and scale effects affecting air bubble entrainment in hydraulic jumps. *In*: M. Sommerfield, ed. *Proceedings of 6th International Conference on Multiphase Flow ICMF 2007*. Leipzig, Germany, 9-13 July 2007, Session 7, Paper S7_Mon_-B_S7_Mon_B_3, 11 pages.

Chanson, H., 2009. Current knowledge in hydraulic jumps and related phenomena. A survey of experimental results. *European Journal of Mechanics B/Fluids*, 28 (2), 191–210. DOI: 10.1016/j.euromechflu.2008.06.004

Chanson, H., 2010. Convective transport of air bubbles in strong hydraulic jumps. *International Journal of Multiphase Flow*, 36 (10), 798–814.

Chanson, H., 2011. Hydraulic. *La Houille Blanche*, 3, 5–16. DOI: 10.1051/lhb/2011026

Chanson, H., 2012. Momentum considerations in hydraulic jumps and bores. *Journal of Irrigation and Drainage Engineering*, 138 (4), 382–385. DOI: 10.1061/(ASCE) IR.1943-4774.0000409

Chanson, H. and Brattberg, T., 2000. Experimental study of the air-water shear flow in a hydraulic jump. *International Journal of Multiphase Flow*, 26 (4), 583–607.

Chanson, H. and Carosi, G., 2007. Advanced post-processing and correlation analyses in high-velocity air-water flows. *Environmental Fluid Mechanics*, 7 (6), 495–508.

Chanson, H. and Chachereau, Y., 2013. Scale effects affecting two-phase flow properties in hydraulic jump with small inflow Froude number. *Experimental Thermal and Fluid Science*, 45, 234–242. DOI: 10.1016/j.expthermflusci.2012.11.014

Chanson, H. and Gualtieri, C., 2008. Similitude and scale effects of air entrainment in hydraulic jumps. *Journal of Hydraulic Research*, 46 (1), 35–44.

Hager, W.H., Bremen, R., and Kawagoshi, N., 1990. Classical hydraulic jump: length of roller. *Journal of Hydraulic Research*, IAHR 28 (5), 591–608.

Henderson, F.M., 1966. *Open channel flow*. New York: MacMillan.

Kucukali, S. and Chanson, H., 2008. Turbulence measurements in hydraulic jumps with partially-developed inflow conditions. *Experimental Thermal and Fluid Science*, 33 (1), 41–53. DOI: 10.1016/j.expthermflusci.2008.06.012

Leandro, J., Carvalho, R., Chachereau, Y., and Chanson, H., 2012. Estimating void fraction in a hydraulic jump by measurements of pixel intensity. *Experiments in Fluids*, 52 (5), 1307–1318. DOI: 10.1007/s00348-011-1257-1

Liggett, J.A., 1994. *Fluid mechanics*. New York: McGraw-Hill.

Lighthill, J., 1978. *Waves in fluids*. Cambridge, UK: Cambridge University Press.

Long, D., Rajaratnam, N., Steffler, P.M., and Smy, P.R., 1991. Structure of flow in hydraulic jumps. *Journal of Hydraulic Research*, IAHR 29 (2), 207–218.

Mossa, M., 1999. On the oscillating characteristics of hydraulic jumps. *Journal of Hydraulic Research*, 37 (4), 541–558.

Mossa, M. and Tolve, U., 1998. Flow visualization in bubbly two-phase hydraulic jump. *Journal of Fluids Engineering, ASME*, 120, 160–165.

Mouaze, D., Murzyn, F., and Chaplin, J.R., 2005. Free surface length scale estimation in hydraulic jumps. *Journal of Fluids Engineering*, Transactions ASME 127, 1191–1193.

Murzyn, F. and Chanson, H., 2009. Experimental investigation of bubbly flow and turbulence in hydraulic jumps. *Environmental Fluid Mechanics*, 9 (2), 143–159.

Murzyn, F., Mouaze, D., and Chaplin, J.R., 2005. Optical fibre probe measurements of bubbly flow in hydraulic jumps. *International Journal of Multiphase Flow*, 31 (1), 141–154.

Murzyn, F., Mouaze, D., and Chaplin, J.R., 2007. Air-water interface dynamic and free surface features in hydraulic jumps. *Journal of Hydraulic Research*, IAHR 45 (5), 679–685.

Rajaratnam, N., 1962. An experimental study of air entrainment characteristics of the hydraulic jump. *Journal of Instruction Engineering India*, 42 (7), 247–273.

Rajaratnam, N., 1965. The hydraulic jump as a wall jet. *Journal of the Hydraulics Division*, ASCE 91 (HY5), 107–132.

Rajaratnam, N., 1967. Hydraulic jumps. *In*: V.T. Chow, ed. *Advances in Hydroscience*. vol. 4. New York: Academic Press, 197–280.

Resch, F.J. and Leutheusser, H.J., 1972. Le ressaut hydraulique: mesure de turbulence dans la région diphasique [The hydraulic jump: turbulence measurements in the two-phase flow region]. *Journal La Houille Blanche*, 4, 279–293, [in French].

Zhang, G., Wang, H., and Chanson, H., 2013. Turbulence and aeration in hydraulic jumps: free-surface fluctuation and integral turbulent scale measurements. *Environmental Fluid Mechanics*, 13 (2), 189–204. DOI: 10.1007/s10652-012-9254-3